1998

Turbidite flux, architecture and chemostratigraphy of the Herodotus Basin, Levantine Sea, SE Mediterranean

MIKE REEDER[1], R. GUY ROTHWELL[2], DORRIK A. V. STOW[1], GISELA KAHLER[2] & NEIL H. KENYON[2]

[1]*Department of Geology, University of Southampton*

[2]*Challenger Division for Seafloor Processes, Southampton Oceanography Centre, Empress Dock, European Way, Southampton, SO14 3ZH, UK*

Abstract: The Herodotus Basin is the deepest part of the SE Mediterranean and receives allochthonous sediments as turbidity currents and debris flows from around its margin. During the late Quaternary, characteristic supply has been from at least four sources. These are (1) dark coloured, calcium carbonate-poor fine-grained turbidites derived from the Nile Cone to the south and south-east, (2) lighter coloured, calcium carbonate-rich, slightly coarser-grained turbidites derived from the Libyan–Egyptian shelf to the south, (3) small, light brown foraminifer-rich, muddy-silty turbidites derived from the Cyprus–Eratosthenes seamount (Anatolian Rise) carbonate shelf to the east, and (4) small localized debris flow deposits derived from the Mediterranean Ridge to the north. During the late Quaternary (0–60 ka), and specifically the period of 0–27 ka, the basin has filled predominantly with allochthonous material derived from the Nile Cone, although one megaturbidite of basin-wide extent was derived from the Libyan–Egyptian shelf. Turbidites have been correlated across the Herodotus Basin using the technique of chemostratigraphy. Matching the results of geochemical analysis may show whether or not the beds in different cores were deposited by the same mass-wasting event, for individual turbidites commonly have diagnostic and unique geochemical 'fingerprints' in terms of major, minor and trace element composition. Sediment budgets for the three main turbidite sources are calculated. The cumulative volume of the sedimentary input for the Nile Cone- derived turbidites over the last 27 ka is *c.* 500 km^3, giving an average sedimentation rate of *c.* 45 cm ka^{-1}, and a volume per unit time of 18 km^3 ka^{-1}. A megaturbidite, derived from the Libyan–Egyptian shelf, is of basin-wide extent and has a volume of *c.* 400 km^3.

As part of the European Union-sponsored MAST II PALAEOFLUX programme, set up to investigate biogeochemical fluxes in the Mediterranean Sea, the RV *Marion Dufresne* (Cruise 81, January–February 1995) collected a total of 30 long piston cores and nine box cores from the Western and Eastern Mediterranean. This paper presents the results of a study based on five of these long piston cores (ranging from 13.7 to 25.8 m in length) recovered from the Levantine Sea in the SE Mediterranean. These cores were taken along a *c.* 325 km long SW–NE transect across the Herodotus Basin (Fig. 1, Table 1). Preliminary results are also presented from interpretation of 3.5 kHz high-resolution seismic profiles collected during the same cruise.

The main purpose of this research is to identify and correlate allochthonous units on the plain, so as to estimate the amount of material being eroded from sediment source areas per unit time, and to quantify downslope transport of terrigenous material onto the plain during the late Quaternary.

Methods

All cores were split and described on the ship. P-Wave velocity (compressional wave) and magnetic susceptibility measurements were then made at 5 cm intervals using the shipboard multi-sensor core logger operated and designed by the geotechnical consultants Geotek Ltd (Haslemere, UK). Detailed re-logging of the cores took place post-cruise together with standard sedimentological analyses for grain size, calcium carbonate content and geochemistry using inductively coupled plasma atomic emission spectroscopy (ICP-AES) and micropalaeontological analysis of foraminifera and nannofossils. Grain-size analyses of 88 sediment samples were made by wet sieving for any sand fraction present and then using a Micromeritics 5100 sedigraph size analyser for measuring the fine fraction (2–63 μm). Calcium carbonate content ($CaCO_3$) was determined by acid treatment of hand-ground material and coulometric detection of CO_2. Replicate analyses and in-house standards were used to control for error.

REEDER, M., ROTHWELL, R. G., STOW, D. A. V., KAHLER, G. & KENYON, N. H. 1998. Turbidite flux, architecture and chemostratigraphy of the Herodotus Basin, Levantine Sea, SE Mediterranean *In*: STOKER, M. S., EVANS, D. & CRAMP, A. (eds) *Geological Processes on Continental Margins: Sedimentation, Mass-Wasting and Stability.* Geological Society, London, Special Publications, **129**, 19–41.

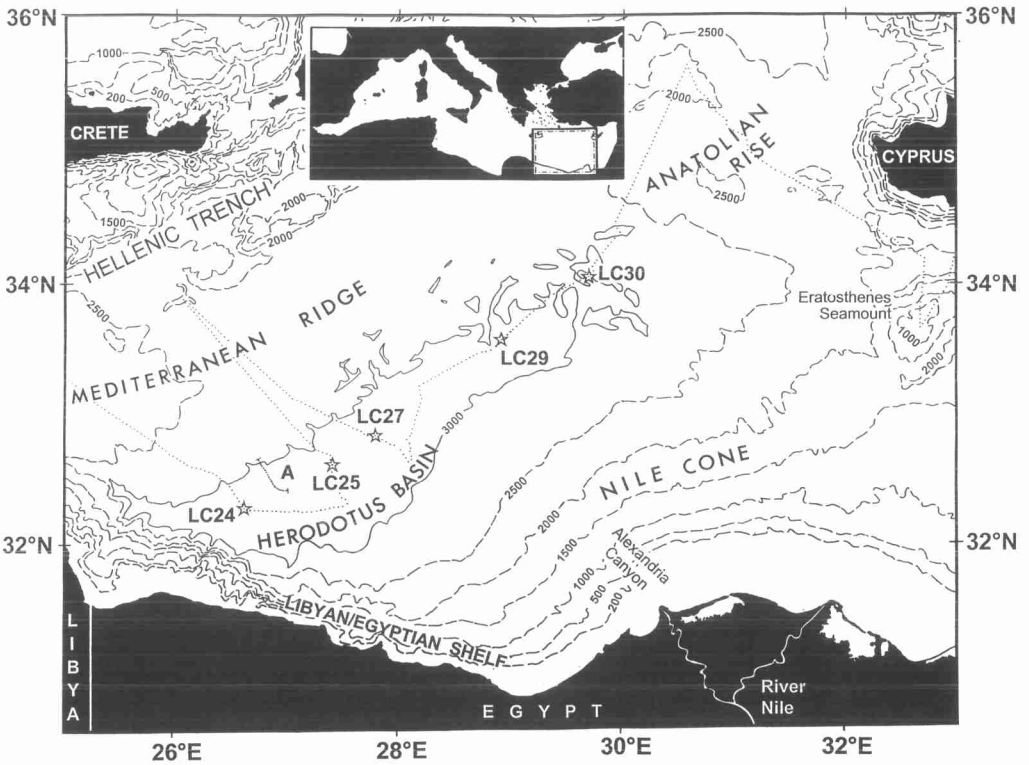

Fig. 1. Location map for the Herodotus Basin showing the bathymetry at 200 m, 500 m, and every 500 m thereafter. The core positions (LC24–LC30) and ships track for RV *Marion Dufresne* Cruise 81 are shown, together with the BAN-82 core (transect A) studied by Cita *et al.* (1984*a*) and Lucchi & Camerlenghi (1993).

Table 1. *Location, depth and length of the five cores from this study (MD-81) and the nine cores from two previous studies (BAN-82) by Cita* et al. *(1984a) and Lucchi & Camerlenghi (1993)*

Core no.	Core type	Water depth (corr. m)	Latitude	Longitude	Core length (m)
MD-81					
LC24	Long piston	3191	32°17.71′N	26°37.95′E	18.31
LC25	Long piston	3129	32°36.01′N	27°23.25′E	13.71
LC27	Long piston	3131	32°48.91′N	27°40.45′E	14.95
LC29	Long piston	3138	33°35.63′N	28°56.32′E	24.66
LC30	Long piston	3144	34°04.70′N	29°42.72′E	25.82
BAN-82					
PC-10	Piston	3198	32°20.55′N	26°58.98′E	11.09
PC-11	Piston	3161	32°26.19′N	26°54.55′E	7.88
PC-12	Piston	3088	32°29.95′N	26°52.62′E	10.92
GC-13	Gravity	3044	32°34.55′N	26°51.00′E	2.58
GC-14	Gravity	3088	32°37.70′N	26°48.14′E	4.31
PC-15	Piston	2915	32°42.60′N	26°44.61′E	10.50
GC-16	Gravity	3008	32°34.42′N	26°50.86′E	4.47
PC-17	Piston	3096	32°32.45′N	26°51.30′E	9.07
GC-18	Gravity	3066	32°32.83′N	26°50.49′E	4.62

Table 2. *The 22 elements measured for geochemical analysis of the turbidite horizons using inductively coupled plasma atomic emission spectroscopy (ICP-AES)*

Element	Units	Measured high count	Measured low count	Al_2O_3 corrected high count	Al_2O_3 corrected low count	Scaling Factor (X)
TiO_2	%	1.65	0.02	0.14	0.06	100.00
Al_2O_3	%	15.77	0.28	–	–	–
Fe_2O_3	%	10.66	0.16	0.73	0.42	10.00
MnO	%	0.73	0.01	0.07	0.004	1000.00
MgO	%	3.73	0.19	0.75	0.20	20.00
CaO	%	39.75	2.12	12.17	0.15	2.00
Na_2O	%	3.13	0.11	0.48	0.15	50.00
K_2O	%	1.97	0.06	0.22	0.07	100.00
P_2O_5	%	0.25	0.02	0.09	0.013	100.00
Ba	ppm	378.48	13.65	56.10	12.93	0.25
Co	ppm	54.80	1.13	8.30	2.00	2.00
Cr	ppm	107.02	1.85	8.94	3.24	2.00
Cu	ppm	105.64	2.03	11.07	2.47	2.00
Li	ppm	57.17	–8.39	–	–	–
Mo	ppm	18.04	–2.72	–	–	–
Ni	ppm	98.56	1.00	9.22	3.54	2.00
Pb	ppm	141.44	–8.96	–	–	–
Sc	ppm	20.02	0.28	1.33	0.95	10.00
Sr	ppm	4254.32	110.99	1302.70	9.87	0.02
Y	ppm	30.20	0.82	3.27	1.60	5.00
Zn	ppm	101.35	2.47	12.00	4.78	1.00
V	ppm	193.60	4.06	15.60	8.59	1.00

The measured high and low count numbers for each element have been corrected by dividing each element by the Al_2O_3 measured value for the separate samples and then scaled by a factor X to fall between 0.00 and 25.00 (Grant 1986). Li, Pb and Mo were disregarded because of their negative low count number.

Just under 200 samples were taken from turbidite beds for analysis of 22 major, minor and trace elements. The analyses were performed using ICP-AES after digestion of 0.5 g of sample with a combination of hydrofluoric, perchloric and nitric acids. Accuracy was checked using standard reference materials and monitored with in-house standards. Precision was better than 5% for all elements. The results were first normalized to their Al_2O_3 value, and then scaled so that a number for the whole range of elements was obtained that fell between zero and 25, following the method of Grant (1986) (see Table 2).

Geological setting and previous work

The Herodotus Basin or Abyssal Plain is an elongate depression in the Eastern Mediterranean defined by the 3000 m isobath. It is bounded to the NW by the accretionary prism complex forming the Mediterranean Ridge and to the SE by the Nile Cone. The shorter SW and NE ends of the basin are bounded by the Libyan–Egyptian continental slope and Anatolian Rise, respectively (Fig. 1). Convergence of the European and African plates has created and deformed the Mediterranean Ridge accretionary prism resulting in complex topography along the NW margin of the basin, whereas growth and progradation of the Nile Cone has occurred across the SE part of the basin. Bathymetric study shows that much of the floor of the basin is no longer a plain in the true sense (as a result of deformation) and therefore the term 'basin' is used rather than 'abyssal plain'.

Two previous papers discussed sedimentary processes and patterns in the Herodotus Basin (Cita *et al.* 1984*a*; Lucchi & Camerlenghi 1993). Both concerned a study based on the RV *Bannock* BAN-82 cruise, during which five piston cores and four gravity cores were collected on a SE–NW transect across the width of the Herodotus Basin and onto the Mediterranean Ridge (Fig. 1). Cita *et al.* (1984*a*) detailed the petrology and sources for two distinct types of turbidites (Type-A and Type-B). The Type-A turbidites have a black plastic mud fraction rich in smectite, a terrigenous silt fraction, and are sourced from the Nile Cone. The light olive grey

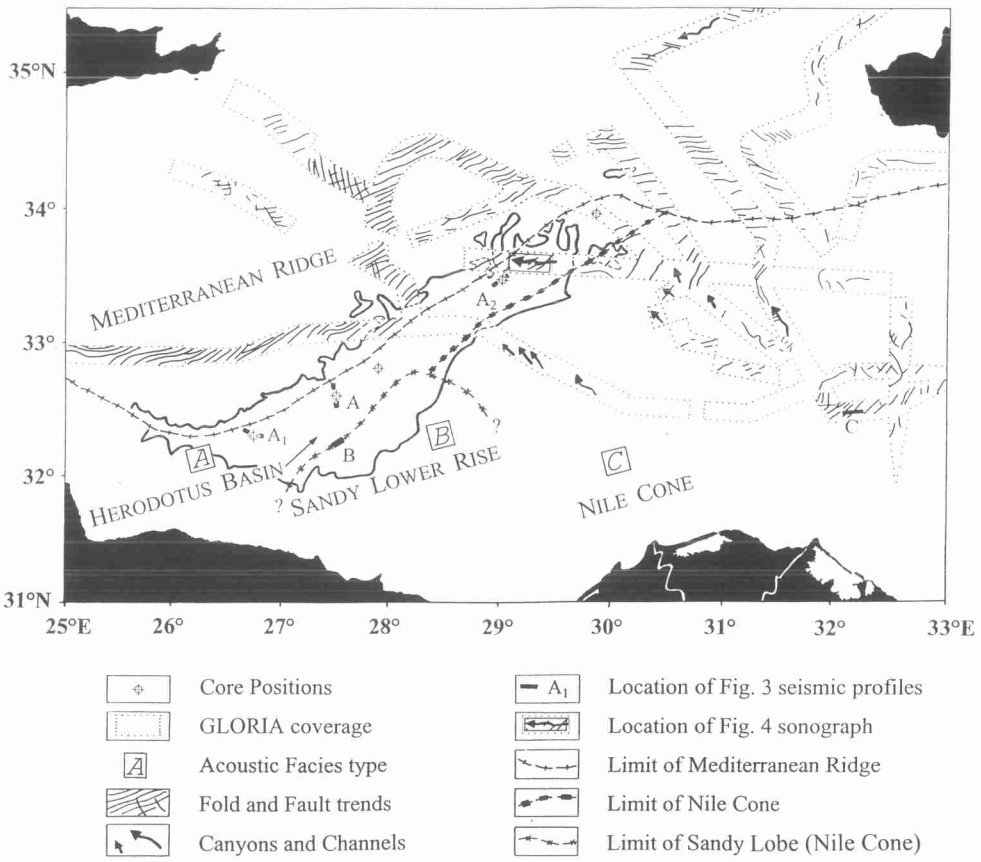

Fig. 2. Acoustic facies–physiographic map of the Herodotus Basin based on analysis of 3.5 kHz data from the RV *Marion Dufresne* Cruise 81 and 12 kHz and GLORIA side-scan sonar data from the RRS *Discovery* Cruises 40, 55 and 104 (Kenyon *et al.* 1975; Stride *et al.* 1977). The 3.5 kHz analysis is after criteria of Jacobi & Hayes (1993). Acoustic facies A–C are explained in the text; profiles shown in Fig. 3 are located. The GLORIA data show the predominant SW–NE trends of folds and faults on the Mediterranean Ridge and the canyon and channel orientations of the Nile Cone. The Herodotus Basin is delineated by the 3000 m isobath (bold line).

Type-B turbidites are coarser grained, carbonate rich with a shallow-water, bioclastic, basal sand poor in smectite, and sourced from the Libyan–Egyptian shelf. A conspicuous megabed termed 'β' by Cita *et al.* (1984*a*), also sourced from the Libyan–Egyptian shelf, was noted with an estimated volume of 10 km^3. Lucchi & Camerlenghi (1993) concluded that the turbidites from the Libyan–Egyptian shelf travelled up the slope of the Mediterranean Ridge for as much as 57 km to a height of 283 m above the basin floor. In addition, the present study has revealed a third turbidite type, 'Type-C', a pale greyish yellow brown, carbonate-rich, foraminifer-rich silty mud sourced from the east towards the Anatolian Rise.

Material derived from the more tectonically active European margin is trapped in the

Fig. 3. Selected 3.5 kHz high-resolution seismic profiles across the Herodotus Basin, showing the characteristics of common echo-types and morpho-acoustic provinces. Profiles are located in Fig. 2. (**a**) Facies A: the deformation front associated with the Mediterranean Ridge accretionary complex showing ponded turbidites between uplifted blocks and ridges. Alongside, 3.5 kHz profiles across sites LC24 and LC 29 (A_1 and A_2, respectively) stationed within the ponded areas, showing thick acoustically transparent layer. (**b**) Facies B: impeded acoustic penetration interpreted as reflecting the presence of a surficial sandy lobe of the Nile Fan. (**c**) Facies C: thinly bedded sub-parallel reflectors from the Nile Cone, with small channels.

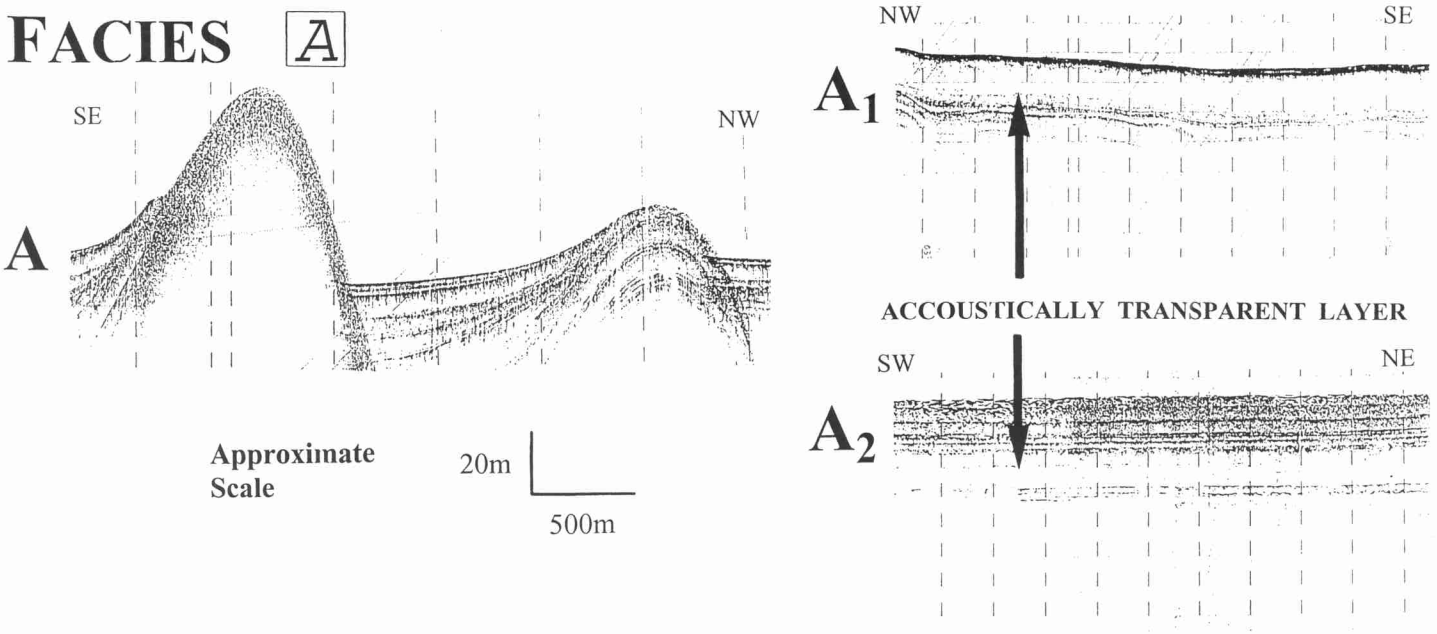
FACIES A
SE
NW
A
Approximate Scale
20m
500m
NW
SE
A1
ACCOUSTICALLY TRANSPARENT LAYER
SW
NE
A2

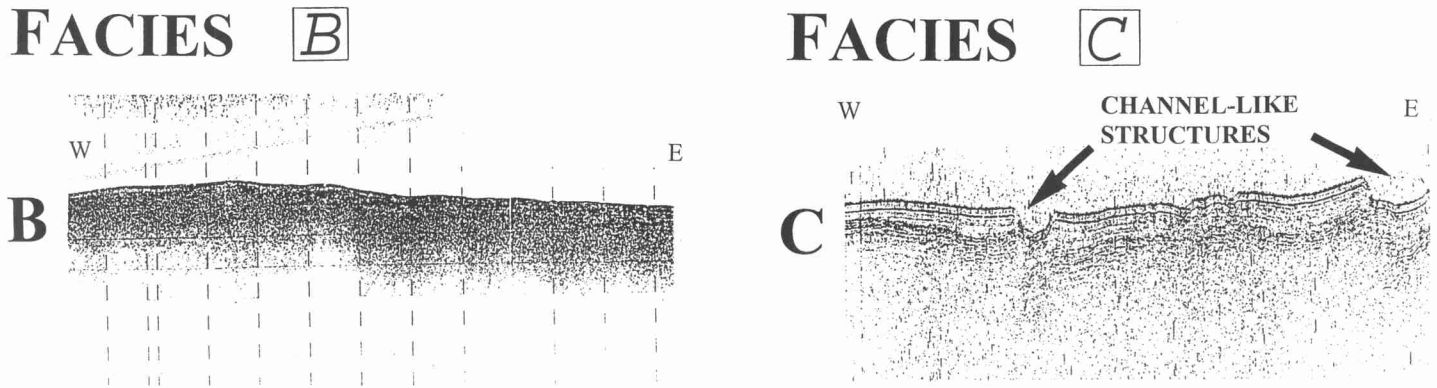
FACIES B
W
E
B
FACIES C
W
CHANNEL-LIKE STRUCTURES
E
C

Hellenic Trench north of the Mediterranean Ridge and consequently cannot reach the Herodotus Basin (Cita *et al.* 1984*a*; Lucchi & Camerlenghi 1993). However, some local downslope reworking from the Ridge itself may occur together with a minor input to the NE end of the basin from the Anatolian Rise.

Morphology and acoustic facies

A preliminary acoustic facies map has been constructed for the Herodotus Basin (Fig. 2) using the 3.5 kHz profiles collected during RV *Marion Dufresne* Cruise MD-81 and GLORIA side-scan sonographs from other cruises in this region (RRS *Discovery* Cruises 40 and 55, Kenyon *et al.* (1975) and Stride *et al.* (1977), respectively). This shows that the truly flat portion of the basin, the abyssal plain, is smaller by approximately half in extent than previously mapped.

Echo types on the 3.5 kHz records have been classified on the basis of clarity and continuity of sub-bottom echoes, the depth of sub-sea-floor penetration by the acoustic signal, and micro-topography (cf. Kidd *et al.* 1985; Jacobi & Hayes 1993). Three acoustic facies or province types have been identified, named A–C.

(A) A morpho-acoustic province consisting of a series of parallel ridges, separated by elongate basins. The Herodotus Abyssal Plain was a true plain in the past, but because of the collision of the African and European plates the northern part of the plain has been deformed into a system of parallel ridges and asymmetric troughs (Fig. 3a). These ridges increase in relief towards the Mediterranean Ridge up to about 100 m above the adjacent plain. Where they have greatest relief they display a hyperbolic echo type with a single, thick, sandy-type reflector, whereas the lower-relief ridges still show deformed but parallel sub-bottom reflectors similar to the flat portion of the plain. Deformation appears to continue to be active, and the developing microtopography clearly interacts with incoming turbidity currents, such that the parallel continuous sub-bottom reflectors of the troughs pinch out and onlap the rising ridges (Fig. 3a).

(B) The second acoustic facies type is a strong prolonged surface reflector with impeded acoustic penetration (Fig. 3b). This is interpreted as part of a sandy, lower-fan lobe system extending from the Nile Cone, based on analogous, but cored echo-types in other areas reported by Jacobi & Hayes (1993) and others.

(C) The third distinct acoustic facies type is the thinly bedded, continuous, sub-parallel reflectors that characterize the Nile Cone (Fig. 3c). The 3.5 kHz seismic profiles show the presence of abundant low-relief channels which incise the thinly bedded sediments (Kenyon *et al.* 1975; Stride *et al.* 1977).

The GLORIA side-scan images show relatively small-scale relief providing widespread evidence of distinctive structural trends on the floor of the Herodotus Basin region (Kenyon *et al.* 1975; Stride *et al.* 1977). The data show that much of the Mediterranean Ridge comprises one or more sets of linear or curvilinear ridge features, some of which lie parallel to the ridge axis (SW–NE) whereas others lie perpendicular to it (NW–SE). The trend of these ridges is also approximately parallel to that of the Herodotus Basin, demonstrating a principal stress orientation, and hence the NW–SE direction of the collision between Africa and Eurasia in this region (Fig. 2).

The side-scan sonar images show a number of channel and canyon trends on the Nile Cone. These are predominantly seen around 33°00′N, 29°30′E trending in a northwesterly direction towards the Herodotus Basin between core sites LC27 and LC29 (Fig. 2). Other meandering channel systems and canyons are seen to the north and north east of this region, radiating from the distal parts of the cone. One such channel, adjacent to core site LC29 (Fig. 4), appears to have encroached into the basin.

The core stations that form the basis for this study were sited on areas of continuous parallel sub-bottom reflectors situated in the troughs between ridges or uplifted blocks (Fig. 3, A_1 and A_2), and represent abyssal plain sediments.

Sediment types

Six main sediment types are recognized in the cores and can be distinguished on the basis of colour, composition, grain size and geophysical properties. The two dominant sediment types are the two contrasting types of turbidites (Type-A and Type-B) first described by Cita *et al.* (1984*a*), whose terminology is retained. The third, Type-C turbidite, is recorded in cores LC29 and LC30, and has similar composition and geophysical properties to the Type-B turbidites. In our study, prominent individual turbidites are identified by letter notation, from turbidite 'p' at the base of the core to turbidite 'a' at the top. Correlation of these turbidites between cores using the above properties has been confirmed by chemostratigraphical techniques (see discussion below). Between individual turbidites there are thin pelagic–hemipelagic intervals and, towards the top of each core, a distinctive dark-coloured sapropel is present. A chaotic, clast-rich mud unit

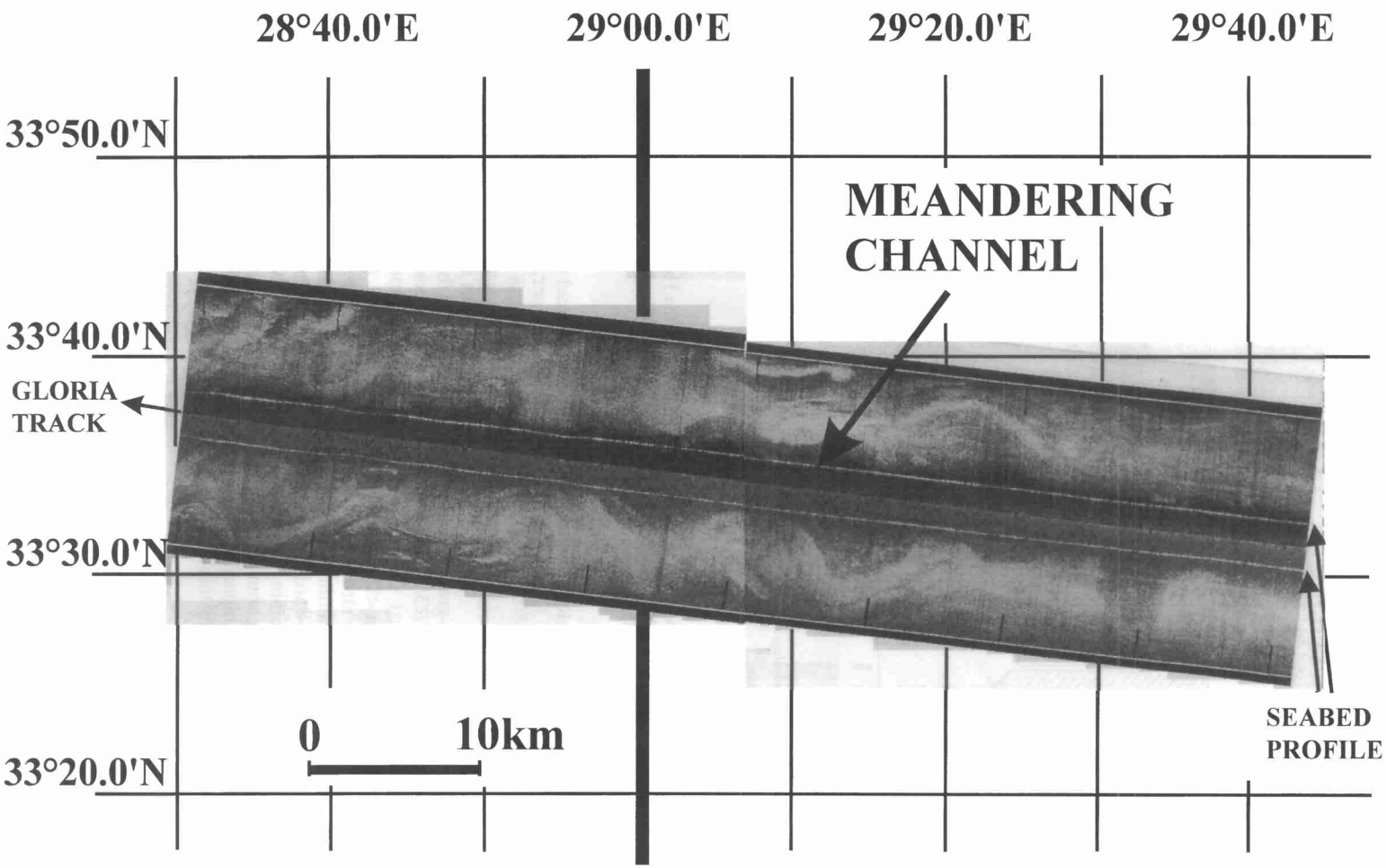

Fig. 4. GLORIA sonograph of a meandering channel–canyon adjacent to core site LC29. (See Fig. 2 for location.)

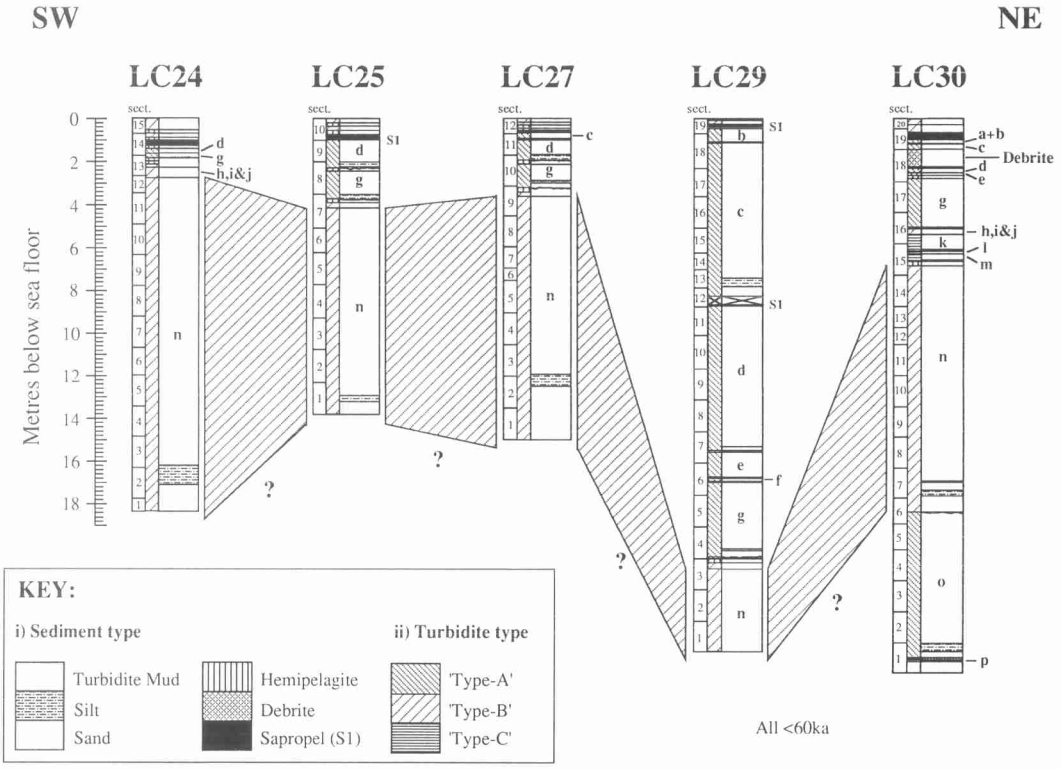

Fig. 5. Lithological logs for the five long piston cores (LC24–LC30) from the Herodotus Basin, showing correlation (oblique hatching) of a thick mud megabed n on the basis of major, minor and trace element geochemistry. The transect length is 325 km.

present in one core (LC30) is interpreted as a muddy debris-flow deposit.

Type-A turbidites

These are mud-rich, dark brown–grey in colour (typical Munsell colour value 10YR3/2, US Geological Survey Rock Color Chart Committee 1991) and range in thickness from <15 cm to >7 m (Fig. 5). Very few sedimentary structures are apparent except weak parallel lamination and discontinuous wavy lamination towards the base of beds. Some of the turbidites contain small iron sulphide nodules (1–5 mm) throughout (Fig. 6a). Type-A turbidites show a broadly bipartite grain-size structure with a thicker upper ungraded or homogeneous mud division (mean size 4–7 μm) overlying a thinner, normally graded basal division, which ranges up to medium–coarse sand (<1 mm) in grain size at the base of thicker beds. These thicker beds also show a subtle oscillation in mean grain size through both divisions (Fig. 7). Type-A beds are best interpreted as fine-grained, distal turbidites, mostly displaying Stow T_5–T_8 turbidite divisions (Stow & Shanmugam 1980; Stow 1985) or Piper E_2–E_3 divisions (Piper & Stow 1991). The coarser basal intervals of some beds belong to Stow T_2–T_4 or Piper E_1 fine-grained turbidite divisions.

Smear-slide examination of the silt and sand fractions of Type-A turbidites shows them to comprise mainly terrigenous quartz, feldspar

Fig. 6. Split-core photographs of sediments and sedimentary structures in selected cores. (a) Fine-grained, randomly spaced millimetric iron sulphide nodules in a dark brown–grey (10YR3/2) Type-A turbidite mud. (b) Base of a light olive–grey (5Y5/2) Type-B turbidite showing laminations. (c) Bioturbated pelagic and hemipelagic sediments with thin graded turbidite layers. (d) Oxidized, laminated and convoluted Type-A turbidite b within S1 Sapropel. (e) The Debrite in LC30, deposited within S1 Sapropel, comprising clasts of Type-A and Type-B turbidites and sapropelic material.

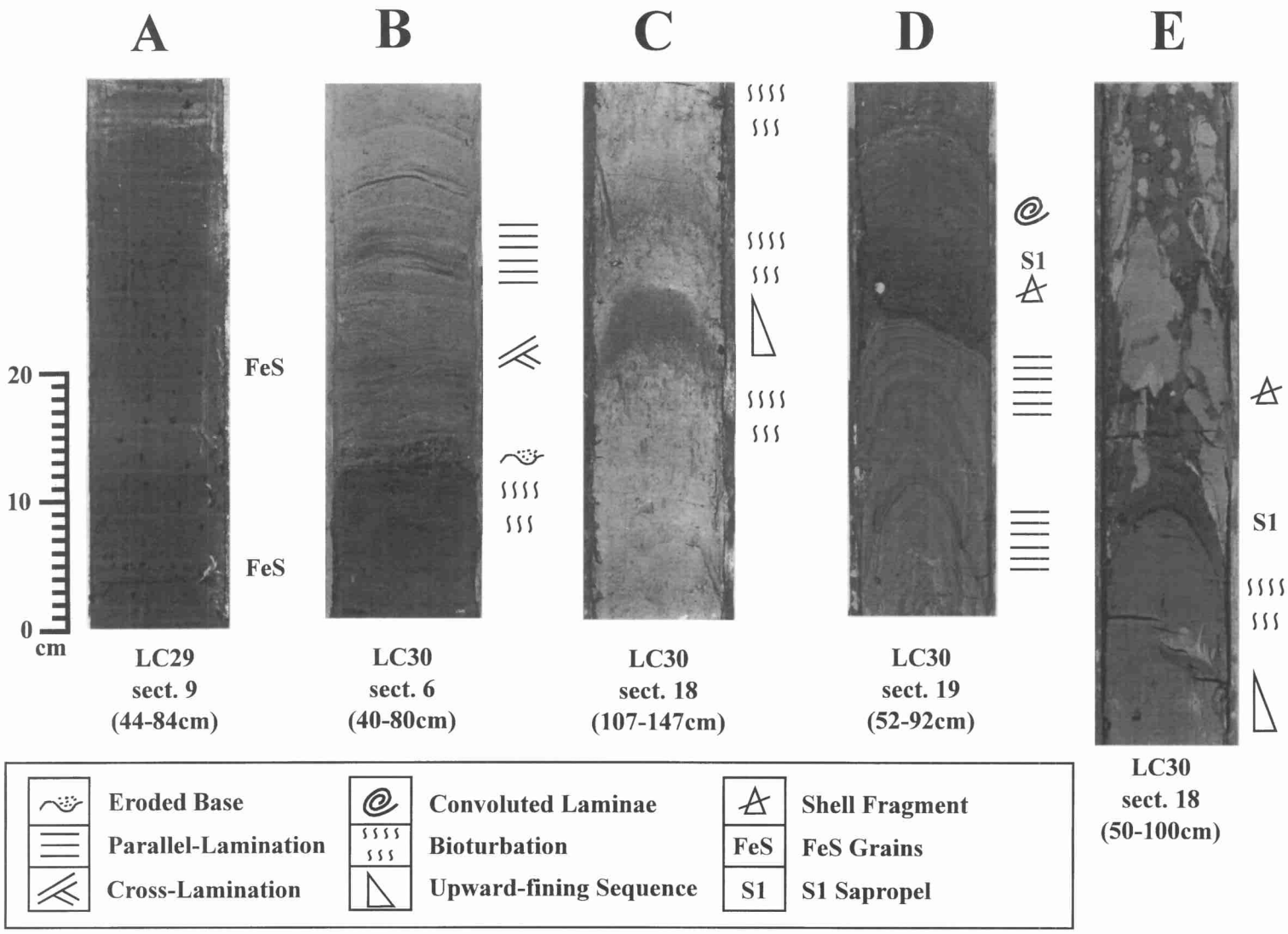
A
B
C
D
E
20
10
0
cm
FeS
FeS
S1
S1
LC29
sect. 9
(44-84cm)
LC30
sect. 6
(40-80cm)
LC30
sect. 18
(107-147cm)
LC30
sect. 19
(52-92cm)
LC30
sect. 18
(50-100cm)
Eroded Base
Parallel-Lamination
Cross-Lamination
Convoluted Laminae
Bioturbation
Upward-fining Sequence
Shell Fragment
FeS Grains
S1 Sapropel

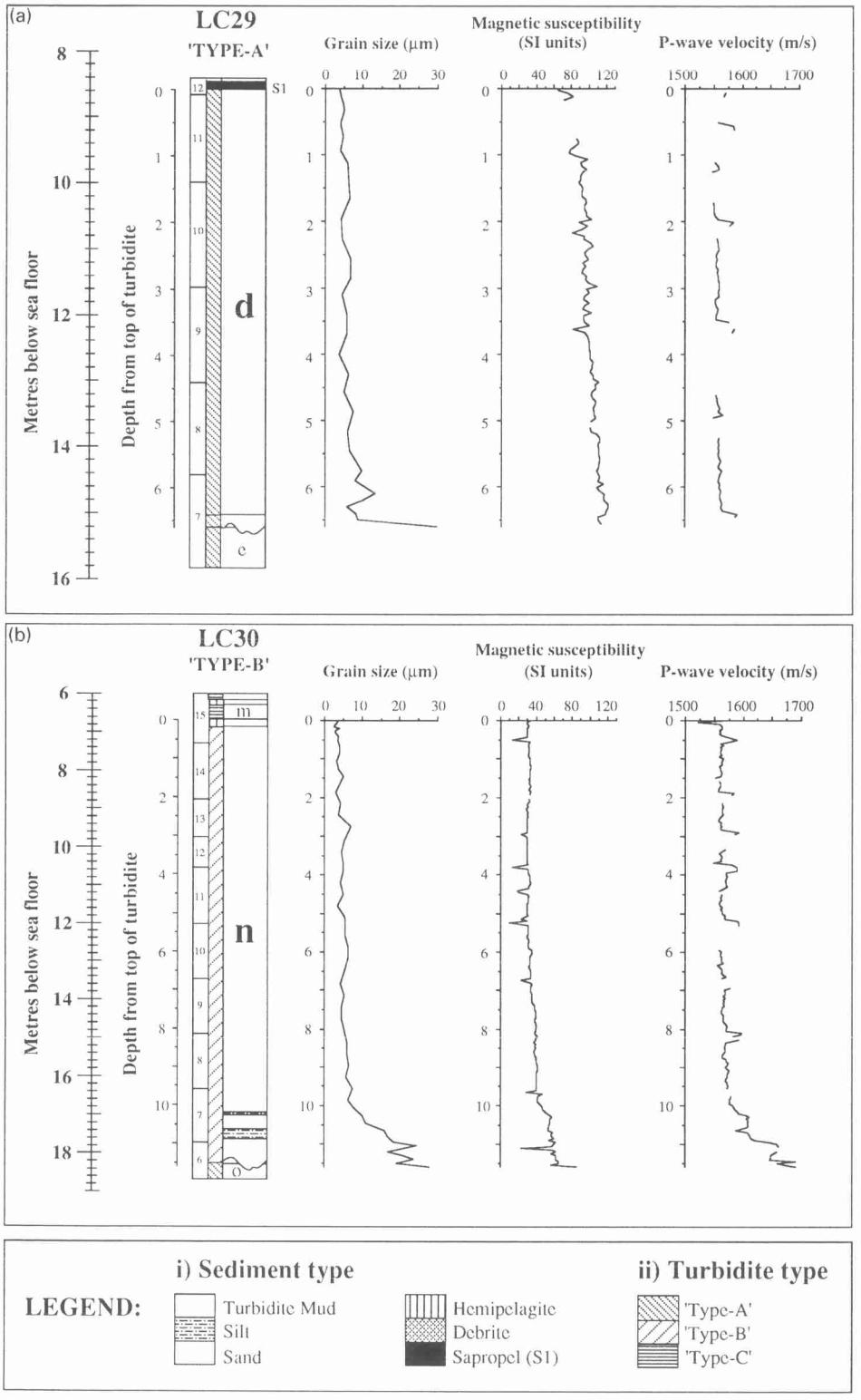
(a)
LC29
'TYPE-A'
Grain size (μm)
Magnetic susceptibility (SI units)
P-wave velocity (m/s)
Metres below sea floor
Depth from top of turbidite
S1
d
e
(b)
LC30
'TYPE-B'
Grain size (μm)
Magnetic susceptibility (SI units)
P-wave velocity (m/s)
Metres below sea floor
Depth from top of turbidite
m
n
o
LEGEND:
i) Sediment type
Turbidite Mud
Silt
Sand
Hemipelagite
Debrite
Sapropel (S1)
ii) Turbidite type
'Type-A'
'Type-B'
'Type-C'

and mica (see Cita *et al.* 1984*a* for detailed analysis). The coarse fraction contains abundant plant debris and other dark organic material. Foraminifera and pteropods are also present in the coarser-grained size fractions. Calcium carbonate content of Type-A turbidites ranges from 4 to 16% (mean 10%), magnetic susceptibility is relatively high (80–150 SI units), and P-wave velocity is around 1550 m s^{-1} (Fig. 8).

Type-B turbidites

The less common Type-B turbidites are a light olive–grey in colour (typical Munsell colour value 10YR6/2) and range in thickness from a few centimetres to >16 m in LC24 (Fig. 5). Like the Type-A turbidites, Type-B are predominantly thick, structureless, homogeneous muds with thinner silty and sandy bases. However, the sand–silt unit at the bottom of cores LC24 and LC27 is >1 m thick and the base of this turbidite was not penetrated. Indistinct parallel lamination occurs in the lower part of the mud division, whereas the sand–silt division may show both parallel and cross-lamination (Fig. 6b). Beds show either a bipartite or tripartite grain-size structure with ungraded mud (4–6 μm) overlying slightly graded mud (4–10 μm) and normally graded silt–sand (up to coarse sand, <1 mm). A slightly irregular oscillation of mean grain size is apparent throughout the large Type-B turbidite n (Fig. 7).

Bed n of the Type-B turbidites is a very thick turbidite or 'megaturbidite', comprising Stow and Piper divisions T_5–T_8 or E_2–E_3, respectively, through the thicker upper mud part, and a coarse-grained sandy base (T_{CD} Bouma divisions, Bouma 1962). Megaturbidites of this sort have been recognized from a number of other Mediterranean basins. For example, the Ionian Sea tsunami-induced 3.5 ka 'Homogenite' of Kastens & Cita (1981) and Cita *et al.* (1984*b*) is a body of homogeneous hemipelagic mud characterized by a thin, normally graded, foraminiferal sand at the base. Similar deposits, such as the Unifites described by Stanley (1980, 1981), have been stripped of the sand fraction through deposition in small slope basins during emplacement, leaving a homogeneous or uniform mud body. The Libyan–Egyptian megaturbidite n shows similar characteristics to those mentioned above, except the sand fraction of the turbidite is thicker than that of the Homogenite and Unifites, and megaturbidite n is a factor of ten times greater in volume.

Analysis of smear slides of the coarse-grained basal sand of megaturbidite n shows quartz, calcite and a high proportion of shelf-derived bioclastic material, such as gastropods, sponge spicules, bivalves, bryzoans, pteropods, and shallow-water benthic and planktonic foraminifera. Some Type-B turbidites also have significant amounts of white and grey pumice grains, dark igneous minerals (e.g. pyroxenes and amphiboles), and cuspate and lunate volcanic glass shards. Calcium carbonate is typically around 50%, magnetic susceptibility values are low (25–45 SI units), and P-wave velocities around 1560–1580 m s^{-1} (Fig. 8).

Type-C turbidites

The rare Type-C turbidites are a moderate yellow–brown in colour (typical Munsell colour value 10YR6/4) and only reach 72 cm (turbidite **k**) and 35 cm (turbidite **m**) in thickness in core LC30 (Fig. 5). These small Type-C turbidites are predominantly structureless, homogeneous muds with centimetre thick-silty and sand-sized foraminifer-rich bases.

Like the Type-B turbidites, the Type-C turbidites comprise Stow and Piper fine-grained turbidite divisions T_5–T_8 or E_2–E_3, respectively, through the thicker upper mud part, and a centimetre-thick T_{CD} Bouma-division medium-grained sandy base.

Analysis of smear slides of the coarse-grained basal foraminiferal sand fractions shows a high proportion of both benthic and planktonic foraminifera (>70%), calcite (10%), muscovite mica (5%) and quartz (5%). There is a small fraction of shelf-derived bioclastic material consisting particularly of gastropods (5%). The Type-C turbidites also have significant amounts of dark igneous minerals (e.g. pyroxenes and amphiboles) and green volcanic glass (<5%). The composition of the Type-C turbidites is very similar to that of the Type-B megaturbidite n, although the colour is much paler. Other differences occur in the calcium carbonate percentages, which are generally lower than the Type-A turbidites at around 40%. The magnetic susceptibility values fall between those of the Type-A and Type-B turbidites (40–45 SI units), and

Fig. 7. Selected downcore parameter profiles for turbidite d (Type-A) and turbidite n (Type-B) in cores LC29 and LC30. Average grain size was measured and is shown against the P-wave velocity and magnetic susceptibility (multi-sensor core logger data).

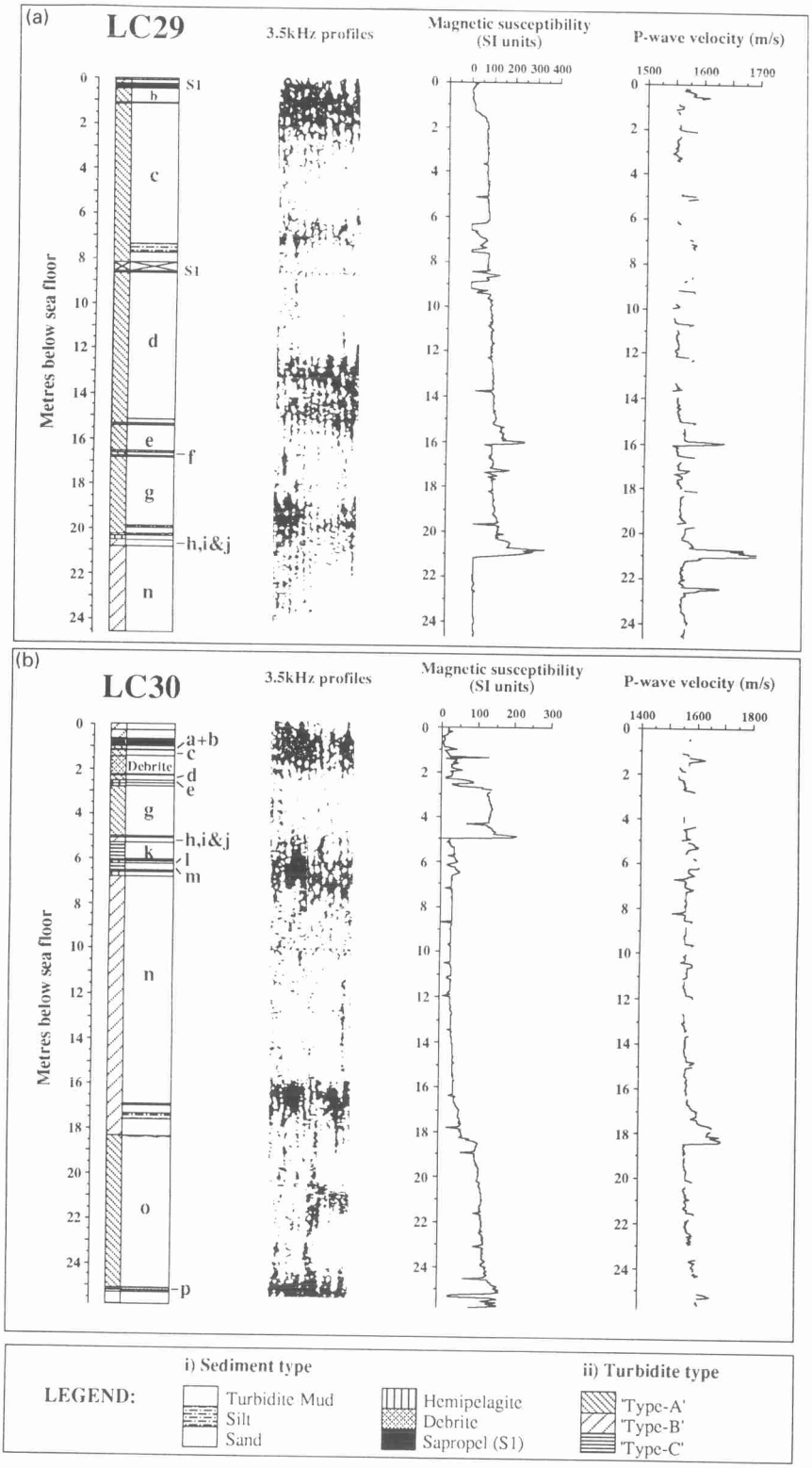
(a)
LC29
3.5kHz profiles
Magnetic susceptibility (SI units)
P-wave velocity (m/s)
Metres below sea floor
S1
b
c
S1
d
e
f
g
h,i&j
n
(b)
LC30
3.5kHz profiles
Magnetic susceptibility (SI units)
P-wave velocity (m/s)
Metres below sea floor
a+b
c
Debrite
d
e
g
h,i&j
k
l
m
n
o
p
LEGEND:
i) Sediment type
Turbidite Mud
Silt
Sand
Hemipelagite
Debrite
Sapropel (S1)
ii) Turbidite type
'Type-A'
'Type-B'
'Type-C'

P-wave velocities are similar at around 1550–1575 m s^{-1}.

Pelagic and hemipelagic deposits

Thin pelagic–hemipelagic intervals occur between many, but not all, turbidite beds. They are typically mixtures of a pale yellowish (10YR6/6) biogenic mud and either brownish grey (10YR3/2) or light olive grey (5Y5/2) muds depending on the nature and colour of the underlying turbidite. They range in thickness from <1 cm to >20 cm, and are characterized by bioturbation and the occurrence of scattered foraminifera throughout (Fig. 6c). Trace fossils include *Chondrites*, *Planolites* and *Phycosiphon*. From their mixed calcareous–terrigenous (quartz and muscovite mica) composition and silty grain size, these sediments may be classified as hemipelagites (Stow *et al.* 1996), although the distinct colour gradation from the underlying turbidites suggests hemiturbidite deposition may have occurred (Stow & Wetzel 1990).

Sapropels

Dark, greyish black (typical Munsell value N0–N1), organic-carbon-rich sediments (C_{org} value >2%, Higgs *et al.* 1994) known as sapropels are well documented from the eastern Mediterranean (e.g. Aksu *et al.* 1995; Thomson *et al.* 1995). A number of thin sapropelic intervals occur in the upper parts of all cores studied from the Herodotus Basin at a cored depth of between 0.2 and 8.7 m. Individual layers range up to 21 cm in thickness and are generally well laminated (Fig. 6d). Some of these layers contain abundant well-preserved pteropods (although in others these are absent), together with warm-water pelagic and benthic foraminifera (Kahler & Dossi 1996, see below). These layers occur interbedded with a variable number and thickness of turbidites in different cores. However, on the basis of faunal content and near-surface occurrence (Kahler & Dossi 1996), they are all considered as part of the same S1 Sapropel interval. The S1 Sapropel has been dated as between 5–6.5 and 9 ka (Bethoux 1993; Higgs *et al.* 1994; Rohling 1994; Aksu *et al.* 1995), and is interpreted as indicating a period of anoxic bottom-water conditions in the Eastern Mediterranean

Debrites

This sediment type occurs only in core LC30 from the northeastern part of the basin. It has been deposited within the S1 Sapropel interval of sections 18 and 19 (Figs 5 and 6e). It is a disorganized mud breccia 82 cm thick, containing irregular to rounded clasts of dark-coloured sapropelic mud and clasts of hemipelagic mud and Type-A, Type-B and Type-C turbidite muds. The sub-rounded–sub-angular clasts are poorly sorted and range in size from <1 cm to 12 cm. Both clasts and matrix generally show plastic deformation structures. Core-parallel elongation of many clasts is apparent, and is interpreted as the result of disturbance during coring. This sediment type is interpreted as a debrite (e.g. Stow & Piper 1984; Stow *et al.* 1996) that seems to be restricted in occurrence to the northern flank of the Herodotus Basin, as were similar debrites noted by Cita *et al.* (1984*a*) and Lucchi & Camerlenghi (1993) during the BAN-82 cruise.

Correlation and dating

To determine the extent and geometry of individual turbidite beds in the Herodotus Basin, and to more accurately estimate turbidite volumes emplaced, three techniques have been used to make a precise correlation between the cores sampled along the 325 km transect.

Geophysical correlation

Generally there is a close correspondence between the distinct, parallel reflectors on the 3.5 kHz high-resolution seismic profiles across the core sites and the contacts between thicker individual turbidite beds, especially where beds are underlain by basal sands (Fig. 8). High-amplitude reflectors mark the bed contacts and/or sandy bases, and acoustically transparent zones typically correlate with the thick structureless turbidite muds. Other geophysical properties, such as P-wave velocity and magnetic susceptibility, further help to characterize individual beds, but resolution of the thinnest beds is not possible on the geophysical records and hence correlation cannot be precise in all cases.

The distinctive megaturbidite n (a Type-B turbidite) correlates with a particularly thick acoustically transparent layer seen on the 3.5 kHz high-resolution seismic profiles that can be

Fig. 8. Geophysical downcore profiles for cores LC29 and LC30 (P-wave velocity and magnetic susceptibility) with corresponding 3.5 kHz high-resolution seismic profiles across the core sites.

traced with confidence over the full length of the basin (Figs 3 and 8). The top of this layer increases in depth from about 2 m below the top of the core in the SW (LC24) to over 21 m below the top of the core towards the NE (LC29), and then shallows to a depth of about 5 m in the extreme NE (LC30). The 3.5 kHz profiles show a very similar pattern to the cores recovered, suggesting that very little of the sediment above the megaturbidite has been lost as a result of the coring process (centimetres rather than metres). The thickness of megaturbidite n, estimated from the 3.5 kHz records using a sediment interval velocity of 1500 m s^{-1}, appears to decrease slightly from *c.* 20 m in the SW (core LC24) to *c.* 10 m in the NE (core LC30). This has proved to be the case when measuring the thickness of sediments above megaturbidite n in the cores (18 m and 11.5 m for cores LC24 and LC30, respectively). Megaturbidite n and other acoustic beds thin markedly against local deformation ridges that characterize the NW part of the basin (Fig. 3b).

There is some evidence from 3.5 kHz profiles that fewer, thicker megaturbidites characterized the late Quaternary. The topmost megaturbidite sampled in our cores was derived from the Libyan–Egyptian shelf, although the underlying megabeds may have been derived from any of the sources. Another three or four megabeds are recognized on the 3.5 kHz seismic profiles, but these were not penetrated by the corer.

Lithological correlation

The broad similarity of sediment types and their distribution in all five cores examined allows a preliminary lithological correlation. The apparent recognition of the Type B megaturbidite n on the 3.5 kHz seismic profiles show this bed's considerable extent. The sapropel layers that occur towards the tops of all five cores are identified as the S1 Sapropel of previous workers, and therefore represent a single dateable horizon (5–6.5 to 9 ka). There is little variation in sediment thickness above this horizon, but in the central and NE parts of the basin (LC27 to LC30) one or more thick turbidites are intercalated with the sapropels.

Geochemical correlation

High-resolution geochemical analysis by ICP-AES of all five Herodotus Basin cores provides a precise correlation tool that is effective over the entire 325 km transect across the Herodotus Basin. Individual turbidite events have their own geochemical signatures (Fig. 9), even though they may share similar colour, compositional, and geophysical properties (cf. Pearce & Jarvis 1992, 1995; Wray & Gale 1993). To assess the degree of geochemical similarity shown by individual turbidites in different cores, cross-plots of the same elements in different cores were made. The regression coefficient of the best fit line so obtained can be used as a measure of similarity.

These multiple-element cross-correlation plots are illustrated for the upper ungraded mud interval (E_3) of two Type A turbidites (Fig. 10a) and two Type B turbidites from cores LC27 and LC25 (Fig. 10b). In each case element concentrations are virtually identical and the beds can be identified as the same in both turbidite d and megaturbidite n (Figs 10a and 10b, respectively). By contrast, poor correlations are seen if the two turbidites compared are not from the same event; this is evident in Fig. 10c, where two unrelated Type-A turbidites are plotted against each other to give a poor coefficient of correlation. The beds were subsequently identified as turbidites g and d, using a combination of the other correlation techniques mentioned above.

However, the grain size of the samples compared must be taken into consideration. Figure 10d is a cross-plot of elements from the mud and sand fractions of the same turbidite, and the correlation is poor. Fine fraction must be compared against fine fraction. Using the same grain-size fraction for comparison allows a possible correlation for each turbidite on a basin-wide basis (Fig. 11).

Dating

Three different methods have been used to estimate the age of beds recovered from the Herodotus Basin: relationship to the S1 Sapropel, micropalaeontological study, and determination of the thickness of pelagic intervals. It is hoped that future stable-isotope work will confirm these preliminary findings.

The S1 Sapropel is well documented throughout the Eastern Mediterranean and dated to between 5–6.5 and 9 ka (Bethoux 1993; Higgs *et al.* 1994; Rohling 1994; Aksu *et al.* 1995). This provides the most recent date in our cores, although some controversy remains concerning the exact termination of this period of anoxia (Higgs *et al.* 1994; Aksu *et al.* 1995). The S3 and older sapropels (S3 is dated at 79 ka, Hilgen, 1991) were not recovered in any of the basin cores used in this study.

Examination of the planktonic foraminifera (Kahler & Dossi, 1996) shows warm-water assemblages in the upper parts of all cores, with

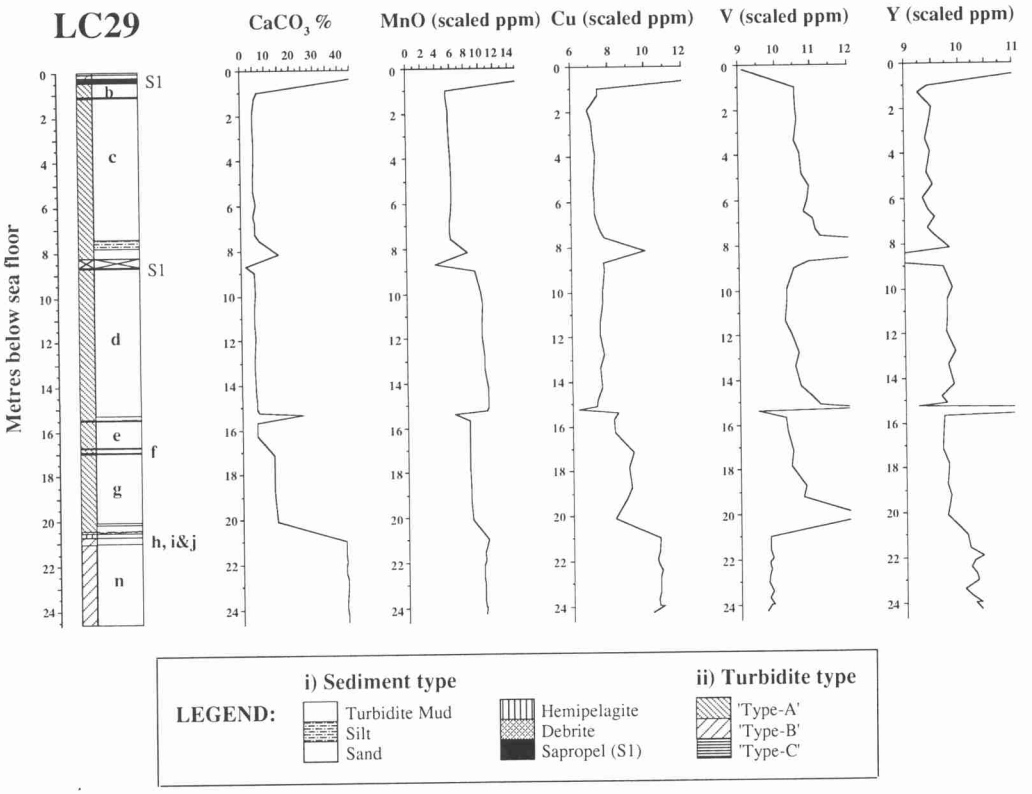

Fig. 9. Selected downcore geochemical profiles for core LC29. Individual turbidites show subtle differences in the concentration of the selected elements. Individual mud beds commonly have diagnostic geochemical 'fingerprints', particularly with regard to minor and trace element composition. The data have been scaled to fall between the values of zero and 25, using the method of Grant (1986).

a very warm-water assemblage in the S1 Sapropel horizon including *Globigerinoides ruber*, *Globigerinoides sacculifer*, *Hastigerina siphoniphera*, *Globigerinoides trilobus trilobus*, *Globigerinoides trilobus immaturus*, *Globigerinoides elongatus*, *Globigerina calida*, *Orbulina universa*, *Globorotalia truncatulinoides* and *Globigerina rubescens*. Turbidites g and e in core LC29 yield both warm- and cold-water species, the latter including left-coiling *G. truncatulinoides* and a high proportion of juveniles. Megaturbidite n also shows a mixed assemblage, whereas turbidite o (core LC30) has a distinctly cold-water fauna including *Globigerina bulloides*, *Globigerina glutinata*, *G. elongatus* and O. *universa*. These data would suggest a Pleistocene–Holocene boundary near the top of turbidite e, assuming a few warmer-water species beginning to return to the Mediterranean as the climate became warmer from *c.* 12–10 ka.

A total of 11 samples were taken for nannofossil analysis from supposed hemipelagic intervals near the base of all five cores. All samples examined contain abundant coccoliths, but some of the material is highly contaminated with older nannofossils as a result of either bioturbation or hemiturbidite processes. However, the assemblage is consistently dominated by *Emiliania huxleyi*, indicating that the pelagic fraction of all samples originates from the late Pleistocene *E. huxleyi* acme interval (Weaver 1983). This places all the recovered section above the earliest part of oxygen isotope stage 3, that is approximately within the last 60 ka.

A first-order estimate of the age at the base of the deepest penetrating core (LC30) can be obtained by adding up the cumulative thickness of pelagic–hemipelagic deposits, and by assuming a constant rate of accumulation for this material, assuming that no erosion by turbidity currents has occurred (cf. Weaver & Kuijpers 1983). Biostratigraphical study of a large number of Eastern Mediterranean cores suggests a rate of *c.* 2.5–3.0 cm ka^{-1} for pelagic sedimentation (E. Rohling, pers. comm. 1996). This places the base of core LC30 at about +27 ka (Table 3).

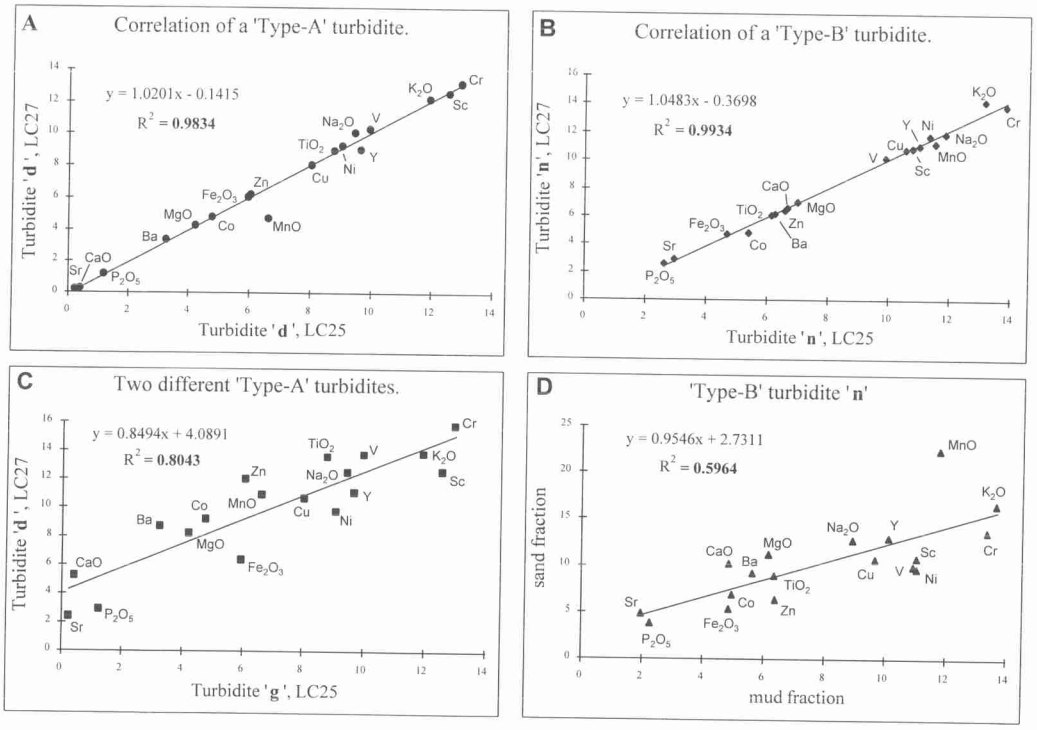

Fig. 10. Isocon diagrams (Grant 1986) for selected turbidite beds, showing the best-fit lines, equations and regression coefficients. Each symbol represents one element as stated in Table 2.

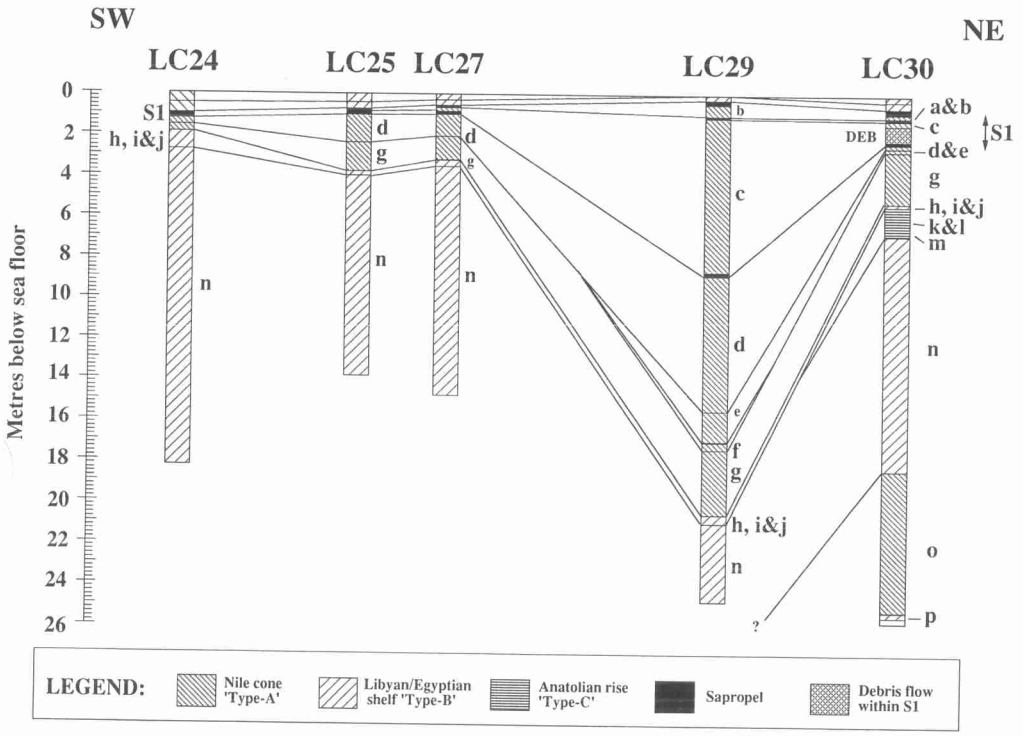

Table 3. *Minimum age calculations for each of the turbidites recorded in the Herodotus Basin*

Turbidite	Type	Present in cores	Max. Thickness (m)	Max. pelagic material between this and overlying turbidite (cm)	Cumulative pelagics down core (cm)	Minimum age (ka)
Turbidite a	A	LC30	0.15	within S1*	–	6.5
Turbidite b	A	LC29 and LC30	0.61	within S1*	–	7.0
Turbidite c	A	All	7.49	within S1*	–	7.5
Debrite		LC30	0.82	within S1*	–	8.0
Turbidite d	A	All	6.69	0.0	0.0	9.0
Turbidite e	A	LC29 and LC30	1.21	8.0	8.0	12.0
Turbidite f	A	LC29	0.20	3.0	11.0	13.5
Turbidite g	A	All	3.43	3.0	14.0	14.5
Turbidite h	B	All	0.14	6.0	20.0	17.0
Turbidite i	B	All	0.07	11.0	31.0	21.5
Turbidite j	B	All	0.06	5.5	36.5	23.5
Turbidite k	C	LC30	0.75	1.0	37.5	24.0
Turbidite l	C	LC30	0.05	6.5	44.0	26.5
Turbidite m	C	LC30	0.35	2.0	46.0	27.5
Turbidite n	B	All	>15.71	0.0?	>46.0	>27.5
Turbidite o	A	LC30	1.79	0.0?	>46.0	>27.5
Turbidite p	B	LC30	0.05	0.0?	>46.0	>27.5

Ages were obtained by using an accumulation rate of 2.5–3.0 cm ka^{-1} (assuming no erosion) and by taking the base of the S1 Sapropel to be 9 ka.
* Dated as being deposited between 5–6.5 and 9 ka (Bethoux 1993; Higgs *et al.* 1994; Rohling 1994; Aksu *et al.* 1995; Thomson *et al.* 1995).

Discussion

The sedimentology, mineralogy and palaeontology of the three types are so different that separate sources have to be considered. The dark brown–grey, fine-grained, quartz, mica and feldspar-rich Type-A turbidites are most probably sourced from the Nile River drainage basin via the Nile Cone (Cita *et al.* 1984*a*; Lucchi & Camerlenghi 1993). The light olive–grey, coarser-grained $CaCO_3$-rich Type-B turbidites, which have negligible terrigenous content, are probably derived from the carbonate-rich Libyan–Egyptian shelf. The moderate yellow–brown, foraminifer- and $CaCO_3$-rich Type-C turbidites are probably derived from the Anatolian Rise to the east of the basin. They cannot be a reworked product of the Type-B megaturbidite n as the Type-C turbidites have small coarse-grained basal fractions which are absent in the thick mud top of the megaturbidite. These proposals for likely provenances are supported by the known dispersal patterns of clay minerals in the sediments of the Eastern Mediterranean Sea (Venkatarathnam & Ryan 1971), and by previous work of Cita *et al.* (1984*a*).

Architecture of the Herodotus Basin fill

The three-dimensional geometry of the three types of turbidite is significantly different (Fig. 11). Megaturbidite n, derived from the Libyan–Egyptian margin, extends across the entire basin, decreasing in thickness from *c.* 18 m in the SW (measured in core LC24 and noted on the 3.5 kHz profiles) to 11.5 m at LC30 in the NE. This apparently uniform decrease in thickness, however, is modified by the ridge–trough system aligned parallel to the length of the basin adjacent to the Mediterranean Ridge. Within each trough segment between adjacent ridges, megaturbidite n is thickest on the NW side, gradually thins across the trough and then thins dramatically to zero as it rises up towards the crest of the lower ridge to the SE (Fig. 3a). This thickness variation is probably due to flow ponding in the deeper part of the asymmetric basins. The flow thins over the gentler flank of the lower ridge but does not rise up the steeper margin of the higher bounding ridge. This further suggests that the flows identified were less thick than the height of the highest ridge (i.e. <100 m).

Fig. 11. Ribbon diagram showing turbidite correlation across the Herodotus Basin. (Note the greater thickness of recent Nilotic turbidites at the site of LC29, suggesting this formed the main depocentre during the late Quaternary.)

By contrast, the post-n turbidites, predominantly derived from the Nile Cone, show a main depocentre centred on 33°36′N, 28°57′E (core LC29) downslope from a fan distributary channel (Fig. 4). These Type-A turbidites thin to the SW and NE, indicating that they were derived from rather smaller flows than megaturbidite n and that individual turbidity currents spread in two directions on entering the plain (or on reaching the NW margin) so that part is seen to the SW and part to the NE. The Coriolis force was clearly insufficient to constrain flow direction only to the right. Many of these thinner flows then travelled the full length of the basin in either direction, although small-volume turbidites, (a and b) are rather more restricted. The post-n sediments are some 21 m thick in LC29, decreasing to about 4 m in thickness at LC27 some 100 km SW, and to about 6 m in thickness at LC30 which is about 80 km to the NE.

During the latter part of the Pleistocene (since at least 27 ka), and the entire Holocene, Nile Cone turbidites represent the main allochthonous input into the basin. Turbidites derived from the Anatolian Rise region to the east (Type-C) are only seen in LC30 in the NE of the basin. The medium-sized turbidites, k and m, have silty, erosive bases but are not seen to extend along the basin in a SW direction. Turbidites of similar sizes or smaller, derived from other sources, are present in other cores in the basin. This may suggest that the mass-wasting events producing the Type-C turbidites k and m were either oblique on entering the basin or were ponded between the deformation ridges, and hence did not proceed down the length of the basin.

Cita *et al.* (1984*a*) and Lucchi & Camerlenghi (1993) showed the extent of the turbidites across the width of the Herodotus Basin towards its SW end. Their sample sites formed a transect from the middle of the basin and onto the Mediterranean Ridge accretionary prism (Fig. 1). Although the cores from the BAN-82 cruise only penetrated a maximum of 12 m, they penetrated older sediments than the cores used in the present study (Fig. 12). These cores show that other Type-A (Nile Cone) and Type-B (Libyan–Egyptian shelf) turbidites from below megaturbidite n were present. Older sapropels (S3–S8) were also recovered. Turbidite n is seen to also be the major event in these cores, with PC-10 showing similar stratigraphical characteristics to those seen in LC24. The Libyan–Egyptian megaturbidite n correlates with the β turbidite described by Cita *et al.* (1984*a*) and Lucchi & Camerlenghi (1993). Although it is not possible to determine an exact correlation between the Nile Cone derived turbidites of Cita *et al.* (1984*a*) in Fig. 12 and those from this study, it is evident that the turbidites become much thinner on the transect from the centre of the Herodotus Basin onto the Mediterranean Ridge.

Cita *et al.* (1984*a*) noted that in two cores (GC-13 and GC-14) the debrites occurred within the S1 Sapropel (Fig. 12). However, in cores taken from farther up the Mediterranean Ridge and farther onto the Herodotus Basin floor, these were absent. These debrites are not thought to originate from the same event as that found in core LC30 at the NE end of the basin. Debrites are generally not as laterally extensive as turbidite deposits and this irregular pattern of deposition could be due to local collapse on the NW flank of the Herodotus Basin from the Mediterranean Accretionary Prism (Fig. 13), or possibly from the smaller tectonically active ridges.

Using the core data from the two studies, together with the 3.5 kHz profiles from this study, it is possible to construct a preliminary isopach map of sediments above the n megabed (Fig. 13). This does not take into account local variations in sediment thickness related to the ridge–trough topography. The main recent depocentre for the Herodotus Basin is seen to be centred around 33°36′N, 28°57′E (LC29). This corresponds to the region of major sediment input from the Nile Cone. This is probably related to the presence of meandering feeder channels providing sediment preferentially to this region as shown by the GLORIA side-scan sonar image in Fig. 4.

Sediment budgets

Summing of pelagic intervals and using an average rate of sedimentation of 2.5–3.0 cm ka^{-1} (E. Rohling, pers. comm. 1996) allows approximate dates for individual turbidite emplacement (Table 3). As the allochthonous beds have been correlated layer-by-layer across the basin using chemostratigraphy, the approximate volumes for each of the larger, laterally extensive turbidites can be calculated (Table 4). Cita *et al.* (1984*a*) placed a rather conservative figure of just 10 km^3 for the volume of the Libyan–Egyptian megabed n. This study revises this figure upward considerably to *c.* 400 km^3, with an average thickness for the turbidite of 10 m and the dimensions covered by the turbidite as a *c.* 100 km in width and 400 km in length. The average frequency of turbiditic emplacement of all types is calculated as one event every 1.6 ka.

The volumes and frequencies of the Type-A Nile Cone turbidites have also been calculated (Table 4), so that sediment budgets can now be determined for the two main sources of

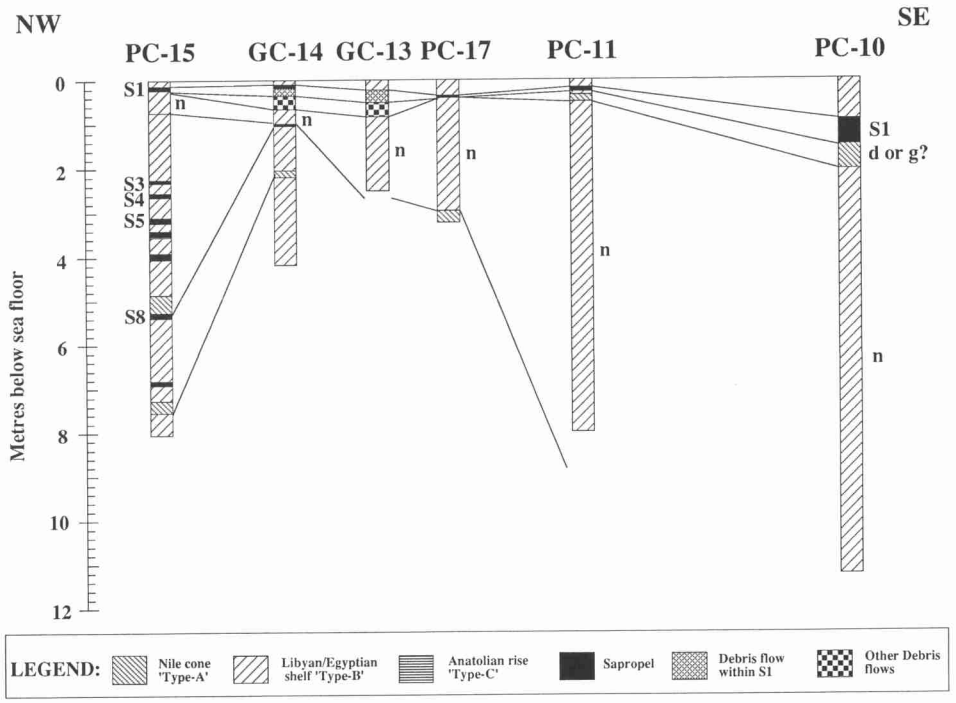

Fig. 12. Schematic ribbon diagram of six of the nine cores recovered by the BAN-82 expedition, adapted from Cita *et al.* (1984*a*) and Lucchi & Camerlenghi (1993). (See Fig. 1 for location of cores.) Turbidite n (this study) correlates with turbidite β of Cita *et al.* (1984*a*).

turbidites. The cumulative volume of the sedimentary input for the Nile Cone source is *c.* 500 km^3, giving an average sedimentation rate of *c.* 45 cm ka^{-1}. The volume per unit time is therefore *c.* 18 km^3 ka^{-1}. The megaturbidite n, of Libyan–Egyptian shelf derivation, has a volume of *c.* 400 km^3. Type-C turbidites, derived from the Anatolian Rise, have a smaller volume of 12 km^3, with a sedimentation rate and volume per unit time of 1 cm ka^{-1} and 0.4 km^3 ka^{-1} respectively.

Sedimentary classification of the late Quaternary turbidite basin fill

Pilkey (1987) discussed the factors that control basin-plain geometry: (a) the arrangement of entry points around the edge of the plain and (b) the ratio of the drainage basin area to the area of basin-plain floor. The Herodotus Basin is dominated by turbidites, including large-scale events, sourced from the Nile Cone, the Libyan/Egyptian carbonate shelf, and the Anatolian Rise (Fig. 13). In Pilkey's classification of basin plains, the entry point configuration for the Herodotus Basin would be Type A, a radial configuration showing entry points from four sources. The drainage basin area of the Nile River is *c.* 1.9 × 106 km^2, and the area of Herodotus Basin plain (below 3000 m isobath) is calculated at *c.* 4×10^4 km^2. This gives a drainage/basin-plain ratio of *c.* 48.

The overall basin fill characteristics for the Herodotus Basin, such as basin area, drainage area, drainage/basin-plain ratio, volume of turbidites, volume per unit time and sedimentation rates, are very similar to those for a number of other basin plains (Pickering *et al.* 1989). For example, Rothwell *et al.* (1992) noted that the Madeira Abyssal Plain was mainly sourced from two compositionally different areas. These are organic-rich turbidites from the African shelf and volcanic-rich from the Canary Islands, with the volcanic source becoming dominant in the basin's later evolution. The Madeira Abyssal Plain is the most well studied of all abyssal plains (e.g. Jones *et al.* 1992; Rothwell *et al.* 1992; Weaver *et al.* 1992, 1995; Masson 1994; Schminke *et al.* 1995) and therefore forms a reference with which others can be compared. The dominant source of basin fill switched in the Madeira Basin, as has that in the Herodotus Basin from a Libyan–Egyptian shelf source to a predominantly Nile Cone source since 27 ka.

Table 4. *Approximate dimensions of the individual turbidites from the Herodotus Basin*

Turbidite	Type	Approximate average thickness (m)	Approximate area* (km^2)		Approximate volume (km^3)	Minimum age (ka)
Turbidite a	A	0.05	2000	(5)	0.1	6.5
Turbidite b	A	0.2	30,000	(75)	6.0	7.0
Turbidite c	A	2.5	32,000	(80)	80.0	7.5
Debrite		0.6	4000	(10)	2.4	8.0
Turbidite d	A	3.5	36,000	(90)	126.0	9.0
Turbidite e	A	0.7	36,000	(90)	25.2	12.0
Turbidite f	A	0.05	2000	(5)	0.1	13.5
Turbidite g	A	2.0	36,000	(90)	72.0	14.5
Turbidite h	B	0.07	32,000	(80)	2.2	17.0
Turbidite i	B	0.03	28,000	(70)	0.8	21.5
Turbidite j	B	0.03	28,000	(70)	0.8	23.5
Turbidite k	C	0.4	20,000	(50)	8.0	24.0
Turbidite l	C	0.02	2000	(5)	0.04	26.5
Turbidite m	C	0.2	20,000	(50)	4.0	27.5
Turbidite n	B	10.0	40,000	(100)	400	>27.5
Turbidite o	A	5.0?	38,000	(95)	190?	>27.5
Turbidite p	B	0.02?	4000	(10)	0.1?	>27.5

* The area of the basin was calculated as an appropriate proportion of 40,000 km^2 (percentage shown in parentheses).

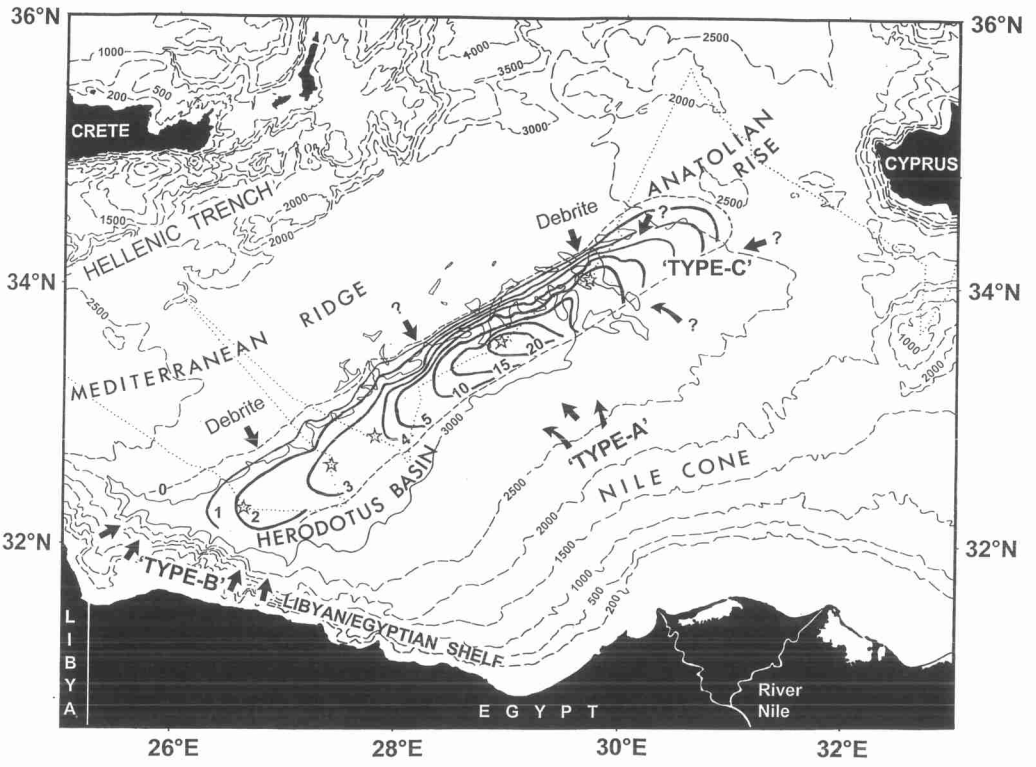

Fig. 13. Isopach map showing the thickness in metres of sediments above the megaturbidite n, the inferred limit of that turbidite, and the location of the late Quaternary depocentre centred on core site LC29. The contour has been drawn using the 3.5 kHz profiles or otherwise estimated from the known bathymetry of the basin.

Table 5. *Comparison of basin characteristics of the Herodotus Basin and the Madeira Abyssal Plain*

Basin characteristics	Madeira Abyssal Plain	Herodotus Basin
Basin area	68,000 km^2	40,000 km^2
Drainage area	3.36×10^6 km^2	1.9×10^6 km^2
Drainage/basin area	49*	48
Volume of turbidites – within depositional period studied	600 km^3	840 km^3
Depositional period studied	300 ka	27.5 ka
Volume/unit time	2 km^3 ka^{-1}*	30.5 km^3 ka^{-1}
Width of bounding continental shelf or slope	1000 km	150 km
Sedimentation rate throughout basin	9 cm ka^{-1}*	83 cm ka^{-1}

* Cf. Rothwell *et al.* (1992).

The sedimentation and volume rates are higher for the Herodotus Basin because of the high sediment supply from the River Nile and the smaller width of bounding shelf–slope compared with that of the Madeira Abyssal Plain (Table 5).

Conclusions

The Herodotus Basin represents the deepest part of the SE Mediterranean and receives allochthonous sediments from turbidity currents primarily from four sediment sources: (1) dark-coloured, fine-grained turbidites from the Nile Cone to the south and southeast, (2) lighter-coloured, $CaCO_3$-rich, slightly coarser-grained turbidites from the Libyan–Egyptian shelf to the southwest, (3) pale, foraminifer- and $CaCO_3$-rich turbidites from the Anatolian Rise region to the east and northeast, and (4) small localized debris flows from the Mediterranean Ridge to the north.

Approximately 50% of the Herodotus Abyssal Plain is no longer bathymetrically a true plain in the conventional sense as a result of neotectonic deformation against the Mediterranean Ridge accretionary prism. Echo-sounding and 3.5 kHz high-resolution seismic profiles collected during RV *Marion Dufresne* Cruise 81 show that part of the SW proximal plain is probably part of the sandy lower rise of the Nile Cone and that the northern part of the plain has been deformed into a belt of small ridges and troughs, up to 100 m in height above the surrounding sea floor. This region, which is at least 40 km in width, and laterally extensive, is interpreted as the deformation front associated with the Mediterranean Ridge accretionary complex.

A megaturbidite derived from the Libyan–Egyptian shelf has been dated at *c.* 27 ka and has an approximate volume of 400 km^3. This does not take into account local variations in sediment thickness related to the ridge–trough topography. The turbidites have been correlated across the Herodotus Basin using major, minor and trace element geochemistry. Each turbidite event has a characteristic geochemical signature allowing excellent chemostratigraphical correlation. Sediment colour, mineralogical and geophysical properties can also be used to correlate the turbidites but the chemostratigraphy provides the most reliable method. This study shows the value of chemostratigraphy as a correlation tool, provided the same size grain fraction is used for analysis.

The main depocentre of the Herodotus Basin for the last 27 ka is centred around 33°36′N, 28°57′E, near the location of core LC29. GLORIA side-scan sonar records show this is related to the presence of meandering channels which provide sediment input to this region from the Nile Cone.

The cumulative volume of the sedimentary input for the Nile Cone is calculated at *c.* 500 km^3, giving an average sedimentation rate of *c.* 45 cm ka^{-1} and a volume per unit time of 18 km^3 ka^{-1}. The small Type-C turbidites derived from the Anatolian Rise contribute little to the Herodotus Basin fill, with a volume of *c.* 12 km^3 and a sedimentation rate of 1.1 cm ka^{-1}.

This work was supported by the European Union Marine Science and Technology Programme (contract MAS2-CT-93-0051) and M.S.R.'s PhD study is NERC funded (award GT4/95/288/E). S. Nixon, N. Higgs and D. Green are thanked for their help in sample preparation and for running geochemical analyses. We also thank A. Dunkley for drafting some of the diagrams and D. Gunn for the geophysical analysis of the core sections using the SOC multi-sensor core logger.

References

Aksu, A. E., Yasar, D. & Mudie, P. J. 1995. Paleoclimatic and paleoceanographic conditions leading to development of sapropel layer S1 in the Aegean Sea. *Palaeogeography, Palaeoclimatology, Palaeoecology*, **116**, 71–101.

BETHOUX, J.-P. 1993. Mediterranean sapropel formation, dynamic and climatic viewpoints. *Oceanologica Acta*, **16**, 127–133.

BOUMA, A. H. 1962. *Sedimentology of some Flysch Deposits: a Graphic Approach to Facies Interpretation*. Elsevier, Amsterdam, 168 pp.

CITA, M. B., BEGHI, C., CAMERLENGHI, A., KASTENS, K. A., MCCOY, F. W., NOSETTO, A., PARISI, E., SCOLARI, F. & TOMADIN, L. 1984*a*. Turbidites and megaturbidites from the Herodotus Abyssal Plain (Eastern Mediterranean) unrelated to seismic events. *Marine Geology*, **55**, 79–101.

——, CAMERLENGHI, A., KASTENS, K. A. & MCCOY, F. W. 1984*b*. New findings of the Bronze age Homogenites in the Ionian Sea: geodynamic implications for the Mediterranean. *Marine Geology*, **55**, 47–62.

GRANT, J. A. 1986. The Isocon diagram – a simple solution to Gresens' equation of metasomatic alteration. *Economic Geology*, **81**, 1976–1982.

HIGGS, N. C., THOMSON, J., WILSON, T. R. S. & CROUDACE, I. W. 1994. Modification and complete removal of Eastern Mediterranean sapropels by postdepositional oxidation. *Geology*, **22**, 423–426.

HILGEN, F. J. 1991. Astronomical calibration of Gauss to Matuyama sapropels in the Mediterranean and implication for the Geomagnetic Polarity Time Scale. *Earth and Planetary Science Letters*, **104**, 226–244.

JACOBI, R. D. & HAYES, D. E. 1993. Northwest African continental rise: effects of near-bottom processes inferred from high-resolution seismic data. *In*: POAG, C. W. & DE CRACIANSKY, P. C. (eds) *Geologic Evolution of the Atlantic Continental Rises*. Van Nostrand Reinhold, New York, 293–326.

JONES, K. P. N., MCCAVE, I. N. & WEAVER, P. P. E. 1992. Textural and dispersal patterns of thick mud turbidites from the Madeira Abyssal Plain. *Marine Geology*, **107**, 149–173.

KAHLER, G. & DOSSI, M. 1996. Micropalaeontology. *In*: ROTHWELL, R. G. (ed.) *R/V* Marion Dufresne *Cruise 81 – Mediterranean giant piston coring transect*. Cruise Report **40–63**.

KASTENS, K. A. & CITA, M. B. 1981. Tsunami induced sediment transport in the abyssal Mediterranean Sea. *Geological Society of America Bulletin*, **92**, 845–857.

KENYON, N. H., BELDERSON, R. H. & STRIDE, A. H. 1975. Plan views of active faults and other features on the Lower Nile Cone. *Geological Society of America Bulletin*, **86**, 1733–1739.

KIDD, R. B., SIMM, R. W. & SEARLE, R. C. 1985. Sonar acoustic facies and sediment distribution on an area of the deep ocean floor. *Marine and Petroleum Geology*, **2**, 210–221.

LUCCHI, R. & CAMERLENGHI, A. 1993. Upslope turbiditic sedimentation on the southeastern flank of the Mediterranean ridge. *Bollettino di Oceanologia Teorica ed Applicata*, **11**, 3–25.

MASSON, D. G. 1994. Late Quaternary turbidity current pathways to the Madeira Abyssal Plain and some constraints on turbidity current mechanisms. *Basin Research*, **6**, 17–33.

PEARCE, T. J. & JARVIS, I. 1992. Applications of geochemical data to modelling sediment dispersal patterns in distal turbidites: Late Quaternary of the Madeira Abyssal Plain. *Journal of Sedimentary Petrology*, **62**, 1112–1129.

—— & —— 1995. High-resolution chemostratigraphy of Quaternary distal turbidites: a case study of new methods for the analysis and correlation of barren sequences. *In*: DUNAY, R. E. & HAILWOOD, E. A. (eds) *Non-biostratigraphical Methods of Dating and Correlation*. Geological Society, London, Special Publications, **89**, 107–143.

PICKERING, K. T., HISCOTT, R. N. & HEIN, F. J. 1989. *Deep Marine Environments: Clastic Sedimentation and Tectonics*. Unwin Hyman, London, 416 pp.

PILKEY, O. H. 1987. Sedimentology of basin plains. *In*: WEAVER, P. P. E. & THOMSON, J. (eds) *Geology and Geochemistry of Abyssal Plains*. Geological Society, London, Special Publications, **31**, 1–12.

PIPER, D. J. W. & STOW, D. A. V. 1991. Fine-grained turbidites. *In*: EINSELE, G. *et al.* (eds) *Cycles and Events in Stratigraphy*. Springer, Berlin, 360–376.

ROHLING, E. J. 1994. Review and new aspects concerning the formation of Eastern Mediterranean Sapropels. *Marine Geology*, **122**, 1–28.

ROTHWELL, R. G., PEARCE, T. J. & WEAVER, P. P. E. 1992. Late Quaternary evolution of the Madeira Abyssal Plain, Canary Basin, NE Atlantic. *Basin Research*, **4**, 103–131.

SCHMINKE, H.-U., WEAVER, P. P. E., FIRTH, J. V., *et al.* 1995. *Proceedings of the Ocean Drilling Program, Initial Reports*, **157**. Ocean Drilling Program, College Station, TX.

STANLEY, J. D. 1980. Mediterranean sedimentation models: carbonate shelves, slope bypassing, ponding, transformation products and "unifites". *In*: WEZEL, F. C. (ed.) *Sedimentary Basin of Mediterranean Margins*. CNR–Urbino University, Urbino, 47–48.

—— 1981. Unifites: structureless muds of gravity-flow origin in the Mediterranean basins. *Geo-Marine Letters*, **1**, 77–83.

STOW, D. A. V. 1985. Fine-grained sediments in deep water: an overview of processes and facies models. *Geo-Marine Letters*, **5**, 17–23.

—— & PIPER, D. J. W. 1984. Deep-water fine-grained sediments: facies models. *In*: STOW, D. A. V. & PIPER, D. J. W. (eds) *Fine-grained Sediments: Deep-water Processes and Facies*. Geological Society, London, Special Publications, **15**, 611–646.

—— & SHANMUGAM, G. 1980. Sequence of structures in fine-grained turbidites: comparison of recent deep-sea and ancient flysch sediments. *Sedimentary Geology*, **25**, 23–42.

—— & WETZEL, A. 1990. Hemiturbidite: a new type of deep-water sediment. *Proceedings of the Ocean Drilling Program, Scientific Results*, **116** Ocean Drilling Program, College Station, TX, 25–34.

——, READING, H. G. & COLLINSON, J. D. 1996. Deep seas. *In*: READING, H. G. (ed.) *Sedimentary Environments: Processes, Facies and Stratigraphy*, Blackwell, Oxford, 395–453.

STRIDE, A. H., BELDERSON, R. H. & KENYON, N. H. 1977. Evolving miogeoanticlines of the East Mediterranean (Hellenic, Calabrian and Cyprus Outer Ridges). *Philosophical Transactions of the Royal Society of London, Series A*, **284**, 255–285.

THOMSON, J., HIGGS, N. C., WILSON, T. R. S., CROUDACE, I. W., DELANGE, G. J. & VAN SANTVOORT, P. J. M. 1995. Redistribution and geochemical behaviour of redox-sensitive elements around S1, the most recent Eastern Mediterranean sapropel. *Geochimica et Cosmochimica Acta*, **59**, 3487–3501.

US GEOLOGICAL SURVEY ROCK COLOR CHART COMMITTEE 1991. *Rock Color Chart*. Geological Society of America, Boulder, CO.

VENKATARATHNAM, K. & RYAN, W. B. F. 1971. Dispersal patterns of clay minerals in the sediments of the Eastern Mediterranean Sea. *Marine Geology*, **11**, 261–282.

WEAVER, P. P. E. 1983. An integrated stratigraphy of the Upper Quaternary of the King's Trough flank area, NE Atlantic. *Oceanologica Acta*, **6**, 451–456.

—— & KUIJPERS, A. 1983. Climatic control of turbidite deposition on the Madeira Abyssal Plain. *Nature*, **306**, 360–363.

——, MASSON, D. G., GUNN, D. E., KIDD, R. B., ROTHWELL, R. G. & MADISON, D. A. 1995. Sediment mass wasting in the Canary Basin. *In*: PICKERING *et al.* (eds) *Atlas of Deep Water Environments: Architectural Style in Turbidite Systems*. Chapman & Hall, London, 287–296.

——, ROTHWELL, R. G., EBBING, J., GUNN, D., & HUNTER, P. M. 1992. Correlation, frequency of emplacement and source directions of megaturbidites on the Madeira Abyssal Plain. *Marine Geology*, **109**, 1–20.

WRAY, D. S. & GALE, A. S. 1993. Geochemical correlation of marl bands in Turonian chalks of the Anglo-Paris Basin. *In*: HAILWOOD, E. A. & KIDD, R. B. (eds) *High Resolution Stratigraphy*. Geological Society, London, Special Publications, **70**, 211–226.